Available online at www.sciencedirect.com

SciVerse ScienceDirect

Ceramics International 38 (2012) 3327–3335

CERAMICS INTERNATIONAL

www.elsevier.com/locate/ceramint

Single step reactive sintering and chemical compatibility between $La_9Sr_1Si_6O_{26.5}$ and selected cathode materials

José M. Porras-Vázquez [a,b], Lucía dos Santos-Gómez [a], Isabel Santacruz [a], Miguel A.G. Aranda [a], David Marrero-López [c], Enrique R. Losilla [a,*]

[a] Dpto. de Química Inorgánica, Cristalografía y Mineralogía, Universidad Málaga, 29071 Málaga, Spain
[b] School of Chemistry, University of Birmingham, B15 2TT Birmingham, United Kingdom
[c] Dpto. de Física Aplicada I, Laboratorio de Materiales y Superficies (Unidad Asociada al C.S.I.C.), Universidad de Málaga, 29071 Málaga, Spain

Received 4 October 2011; received in revised form 7 December 2011; accepted 17 December 2011
Available online 27 December 2011

Abstract

Apatite-type silicates are considered as promising electrolytes for solid oxide fuel cells (SOFC). However more studies on the chemical compatibility of these materials with common SOFC electrodes are required. Here, we report the synthesis of single phase $La_9Sr_1Si_6O_{26.5}$ composition by reactive sintering at 1650 °C for 10 h. Fully dense pellets showed very high oxide-anion conductivity, 25 mS cm^{-1} at 700 °C. Furthermore, the chemical compatibility of $La_9Sr_1Si_6O_{26.5}$ with some selected cathode materials has also been investigated. The lowest reaction temperatures were determined to be 1100 °C, 1000 °C and 900 °C for $La_{0.8}Sr_{0.2}MnO_{3-\delta}$, $La_2Ni_{0.8}Cu_{0.2}O_4$ and $La_{0.6}Sr_{0.4}Co_{0.8}Fe_{0.2}O_3$, respectively. The segregation of minor amounts of SiO_2 seems to be a key limiting factor that must be overcome. Finally, these cathode materials were deposited over dense oxy-apatite pellets and the area specific resistances in symmetrical cells were determined. These values, at 700 °C, were 14.4 and 2.6 Ω cm^2 for $La_{0.8}Sr_{0.2}MnO_{3-\delta}$ and $La_{0.6}Sr_{0.4}Co_{0.8}Fe_{0.2}O_{3-\delta}$, respectively. Furthermore, the area specific resistances are notably improved 0.6 Ω cm^2 when a 50 wt.% composite of $La_{0.6}Sr_{0.4}Co_{0.8}Fe_{0.2}O_{3-\delta}$ and $Ce_{0.8}Gd_{0.2}O_{1.9}$ is used.
© 2011 Elsevier Ltd and Techna Group S.r.l. All rights reserved.

Keywords: Apatite-type electrolyte; SOFC; Chemical compatibility; Area-specific resistance

1. Introduction

Solid oxide fuel cells (SOFCs) are one of the most promising types of fuel cell for large scale power generation and combined heat and power applications. SOFCs offer many advantages over classical combustion-based power generation technologies and have been intensively studied for many years [1–4]. Yttria-stabilized zirconia, YSZ, is the oxide-conducting electrolyte used in the commercial systems. One significant disadvantage of ZrO_2-based SOFCs is the temperature of operation at which ionic conductivity is sufficiently high for practical applications, usually 800–1000 °C.

The oxy-silicates with apatite-type structure and composition $La_{10-x}(SiO_4)_6O_{2\pm\delta}$ have been proposed as alternative electrolytes for SOFCs, exhibiting higher ionic conductivity compared to the YSZ in the intermediate temperature range (500–800 °C), combined with moderate thermal expansion coefficients and very low electronic conductivity [5–11]. Numerous works, including theoretical atomistic simulations [12–14] and neutron powder diffraction [15,16], show that the ionic conduction occurs mainly via interstitial oxide migration both parallel and perpendicular to the channels [14] and it increases with the oxygen concentration in the lattice.

One of the limitations for the practical application of apatite-type silicates as solid electrolytes is the high sintering temperature, which usually ranges between 1600 and 1700 °C. Different synthesis routes have been used to obtain dense ceramics, such as hot-pressing [17], sol–gel [18,19] and freeze-dried precursors and spark-plasma sintering [20]. However, the densification route may alter the conducting properties and the relationship between ceramic microstructure and the grain boundary resistance to the oxide ion conductivity remains to be established.

* Corresponding author. Tel.: +34 952134234; fax: +34 952131870.
E-mail address: r_losilla@uma.es (E.R. Losilla).

0272-8842/$36.00 © 2011 Elsevier Ltd and Techna Group S.r.l. All rights reserved.
doi:10.1016/j.ceramint.2011.12.042

On the other hand, chemical incompatibility between apatite-type silicates and commonly used electrode materials has also been reported. For instance, Tsipis et al., studied the electrochemical stability of $La_{10}Si_5Al_1O_{26.5}$ with several cathode materials: $La_2Ni_{0.8}Cu_{0.2}O_{4+\delta}$, $La_2Ni_{0.8}Cu_{0.2}O_{4+\delta}$–Ag cermet, $La_{0.8}Sr_{0.2}Fe_{0.8}Co_{0.2}O_{3-\delta}$–$Ce_{0.8}Gd_{0.2}O_{2-\delta}$, and $La_{0.7}Sr_{0.3}MnO_{3-\delta}$–$Ce_{0.8}Gd_{0.2}O_{1.9}$ composites [21]. Relatively low performances of these electrodes were achieved in this work, mainly associated with surface diffusion of silica from the electrolyte to the electrodes. Ruddlesden–Popper phases, $LaSr_2Mn_{1.6}Ni_{0.4}O_{7-\delta}$, $La_2Ni_{0.5}Cu_{0.5}O_{4+\delta}$, $LaSr_2Mn_{1.6}Ni_{0.4}O_{7-\delta}$, $La_4Ni_{3-x}Cu_xO_{10-\delta}$ and $La_{3.95}Sr_{0.05}Ni_2CoO_{10-\delta}$; and perovskite phases, $SrMn_{0.6}Nb_{0.4}O_{3-\delta}$, $Sr_{0.7}Ce_{0.3}Mn_{0.9}Cr_{0.1}O_{3-\delta}$ and $Gd_{0.6}Ca_{0.4}Mn_{0.9}Ni_{0.1}O_{3-\delta}$ have also been tested with $La_{10}Si_5Al_1O_{26.5}$. However, a poor electrochemical performance was again observed, partly associated with a strong cation interdiffusion between the materials [22,23]. Bonhomme et al. tested $La_9Sr_1Si_6O_{26.5}$ with $La_{0.75}Sr_{0.25}Mn_{0.8}Co_{0.2}O_{3-\delta}$, and no reactivity between apatite and perovskite materials was observed [24]. However the electrode resistance decreased by increasing the cathode porosity and with the use of a perovskite–apatite composite as a cathode material. The same electrolyte has also been studied with $Nd_{1.95}NiO_{4+\delta}$ cathode and no apparent chemical reactivity was found between both materials [25]. Recently, Marrero-López et al. carried out a compatibility study of $La_{10}Si_{5.5}Al_{0.5}O_{26.75}$ with several electrode materials commonly used in SOFCs, i.e. $La_{0.8}Sr_{0.2}MnO_{3-\delta}$, $La_{0.7}Sr_{0.3}FeO_{3-\delta}$ and $La_{0.6}Sr_{0.4}Co_{0.2}Fe_{0.8}O_{3-\delta}$, as cathodes; and NiO–CGO composite, $La_{0.75}Sr_{0.25}Cr_{0.5}Mn_{0.5}O_{3-\delta}$ and Sr_2MgMoO_6 as anodes. In general, bulk reactivity between the electrodes and the electrolyte was not observed. However the area-specific polarisation resistance (ASR) of these electrodes increased significantly by increasing the sintering temperature, indicating some reactivity at the electrolyte/electrode interface. This effect was minimised using a ceria buffer layer between the electrolyte and electrode materials, obtaining a SOFC with relatively high performance for 100 h of operation [26].

In this work, fully dense $La_9Sr_1Si_6O_{26.5}$ ceramics were prepared by reactive sintering in a single thermal treatment with the total conductivity of 2.5×10^{-2} S cm^{-1} at 700 °C. Furthermore, its potential use as solid electrolyte for SOFC has been evaluated. Chemical compatibility and area-specific resistance, with several electrode materials, have been investigated by X-ray powder diffraction, energy dispersive spectroscopy and impedance spectroscopy measurements.

2. Experimental

2.1. Synthesis-sintering conditions

$La_9Sr_1Si_6O_{26.5}$ samples were prepared by reaction sintering, RS, using high purity oxides: La_2O_3 (Alfa, 99.999%), $SrCO_3$ (Alfa, 99.99%) and SiO_2 (ABCR, quartz powder, 99.31%). Lanthanum oxide was precalcined at 1000 °C for 2 h in order to achieve decarbonation. Reagents were ground for 30 min in an agate mortar, pelletized (500 MPa, ~10 mm diameter and ~1 mm thickness) and heated in air at 1650 °C for 5, 10 and 20 h at a heating/cooling rate of 5 °C min^{-1}. These samples are hereafter labelled as RS_t^T, where T and t indicate the sintering temperature (°C) and time (h) respectively. Compaction (% theoretical density) was calculated taking into account the mass, volume of the pellets and the crystallographic density obtained from the powder diffraction study.

$La_2Ni_{0.8}Cu_{0.2}O_{3-\delta}$ (LNC) and $La_{0.6}Sr_{0.4}Co_{0.8}Fe_{0.2}O_{3-\delta}$ (LSCF) cathode materials were prepared by sol–gel citrate precursor methods. The synthesis procedure was similar to that previously reported [27–29]. Commercial powders of $La_{0.8}Sr_{0.2}MnO_{3-\delta}$ (cathode) (LSM, Praxair specialty ceramics) and $Ce_{0.8}Gd_{0.2}O_{1.9}$ (electrolyte) (CGO, Rhodia) were also used. Furthermore, a composite of 60 wt.% of LSCF and CGO was prepared by mixing the corresponding powders in an agate mortar using acetone as grinding/mixing improving agent.

2.2. Powder diffraction

X-ray powder diffraction (XRPD) patterns were recorded with a X'Pert MDP PRO diffractometer (PANalytical) equipped with a Ge(1 1 1) primary monochromator, using monochromatic Cu Kα_1 radiation (λ = 1.54059 Å) and the X'Celerator detector. The overall measurement time was approximately 4 h per pattern to have good statistics over the 10–100° (2θ) angular range, with 0.017° step size. XRPD studies were also performed to evaluate the chemical compatibility of the apatite-type electrolyte with the different electrodes. The electrolyte and electrodes powders were ground in a 1:1 wt.% ratio in an agate mortar and then fired between 700 and 1300 °C for 24 h in air. All Rietveld quantitative phase analyses (RQPA) were carried out using the GSAS suite of programs [30]. Final global optimised parameters were: background coefficients, zero-shift error, cell parameters and peak shape parameters using a pseudo-Voigt function [31] corrected for axial divergence [32]. The atomic parameters were not refined.

2.3. Microstructural characterization

The morphology of the sintered pellets was studied using a JEOL SM 840 scanning electron microscope. The ceramic surfaces were polished with diamond spray from 6 to 1 μm of diameter and then thermally etched at 50 °C below the sintering temperature for 15 min at a heating/cooling rate of 5 °C min^{-1}. Finally, the samples were gold sputtered for better image definition. Average grain size of sintered pellets was estimated from SEM micrographs using the linear intercept method from at least 30 random lines and three different micrographs with the help of image-analysis software. In addition, the microstructure between the electrode and electrolyte layers and/or any evidence of degradation after electrochemical tests were studied using a JEOL SM-6490LV scanning electron microscope combined with energy dispersive spectroscopy (EDS).

2.4. Conductivity and area-specific resistance measurements

Platinum electrodes were made by coating opposite pellet faces of the dense $La_9Sr_1Si_6O_{26.5}$ pellets with METALOR®

6082 platinum paste and gradually heating to 950 °C for 15 min at a rate of 10 °C min^{-1} in air to decompose the paste and harden the Pt residue. Successive treatments were made to achieve an electrical resistance on both pellet faces lower than 1 Ω. Impedance spectroscopy data were collected in air using a HP4284A impedance analyser over the frequency range from 20 Hz to 1 MHz with an applied voltage of 0.1 V. Electrical measurements were taken on heating and cooling in the temperature range of 200–1000 °C every 25 °C (accuracy of ±1 °C) at 10 °C min^{-1} with a delay time of 30 min at each temperature to ensure thermal stabilization. Measurements were controlled by the winDETA package of programs [33].

For area-specific resistance measurements, symmetrical electrodes were coated on both sides of the dense $La_9Sr_1Si_6O_{26.5}$ pellets using a suspension prepared with the different electrode powders and Decoflux™ (WB41, Zschimmer and Schwarz) as binder material. The symmetrical cells were fired at 950 °C for LSCF, 1000 °C for LSCF–CGO composite and 1100 °C for LSM and LNC cathodes for 1 h in air. Afterwards, a Pt-based ink was applied onto the electrodes to obtain a current collector layer and finally fired at 950 °C for 15 min.

The area-specific resistance (ASR) values were obtained under symmetrical atmospheres (air or humidified 5% H_2–Ar) in a two electrodes configuration [26]. Impedance spectra of the electrochemical cells were collected using a Solartron 1260 FRA, at open circuit voltage (OCV), in the 0.01–10^6 Hz frequency range with an ac signal amplitude of 50 mV. The spectra were fitted to equivalent circuits using the ZView software [34], which allows an estimation of the resistance and capacitance associated with the different contributions.

3. Results and discussions

3.1. Sintering conditions, microstructure and conductivity of $La_9Sr_1Si_6O_{26.5}$

Reaction sintering is a particular type of sintering process in which both chemical reaction of the starting compounds and densification are achieved simultaneously in a single heating step. It has been employed to simplify the processing of the ceramic pellets. Recently, ceramics such as $BaTi_4O_9$, $Ba_5Nb_4O_{15}$, $Sr_5Nb_4O_{15}$ and apatite-type materials were successfully prepared/densified by reaction sintering [35–41]. However, this method may show some shortcomings including the risk of chemically inhomogeneous products due to incomplete reaction of the reactants and difficulties in controlling the microstructure. In this study, three $La_9Sr_1Si_6O_{26.5}$ samples were obtained at a sintering temperature of 1650 °C and different dwell times: 5, 10 and 20 h. After sintering, the pellets were ground and studied by XRPD and their patterns were analyzed by the Rietveld method using the structural description previously reported for $La_{8.65}Sr_{1.35}(SiO_4)_6O_2$, in *P63/m* space group [15], as starting model. The occupation factors for the cation sites were conveniently modified to account for the stoichiometry. Final Rietveld refinements showed good figures of merit with R_F ranging between 3% and 4%. Final refined unit cell parameters and compactions are given in Table 1.

Samples sintered for 5 h, RS_5^{1650}, showed unreacted La_2O_3 and relative density of 88%. Excessive sintering times, i.e. RS_{20}^{1650}, led to single phase but fragile pellets with 93% of relative density. The best sintering conditions were reached for samples prepared at 1650 °C for 10 h (RS_{10}^{1650}) with relative density of 96%. Fig. 1 shows a SEM micrograph obtained for RS_{10}^{1650}. The pellet has low porosity with no visible formation of phase segregations. The SEM micrograph was analyzed to evaluate the grain size distribution and the corresponding average grain size. The grain size showed a Gaussian distribution with an average grain size of 7 μm (inset of Fig. 1).

Impedance spectroscopy was used to determine the electrical conductivity of the pellet with the highest relative density, RS_{10}^{1650}. Representative impedance data at 750 °C is shown as an impedance complex plane plot in Fig. 2. At low temperatures (not shown), a set of overlapping semicircles were observed, likely due to the grain interior (bulk) and internal interfaces (grain boundary and porosity contribution). Lower frequency processes due to electrode contribution were observed in the form of a spike. At 750 °C (inset Fig. 2) the spike collapses to a semicircular arc, indicating that oxygen molecules are able to diffuse through the entire thickness of the electrode. In order to estimate bulk and grain-boundary conductivities of the sample, complex impedance spectra were analyzed by nonlinear least squares fittings of equivalent circuits using the program ZView [34]. The errors obtained for

Table 1
Composition and cell parameters at room temperature for the different electrolyte and electrode materials. Relative density (% TD) of the sintered pellets are also given.

Composition	Abbreviation	*a* (Å)	*b* (Å)	*c* (Å)	*V*/*Z* (Å^3)	% TD
$La_9Sr_1Si_6O_{26.5}$	[a]RS_5^{1650}	9.7076(4)	–	7.2184(3)	589.11(6)	88
	RS_{10}^{1650}	9.7056(1)	–	7.2165(1)	588.72(4)	96
	RS_{20}^{1650}	9.7047(1)	–	7.2172(1)	588.66(1)	93
$La_{0.8}Sr_{0.2}MnO_3$	LSM	5.4751(4)	7.7655(8)	5.5176(4)	234.59(2)	–
$La_2Ni_{0.8}Cu_{0.2}O_4$	LNC	3.8563(1)	–	12.7676(2)	189.87(1)	–
$La_{0.6}Sr_{0.4}Co_{0.8}Fe_{0.2}O_3$	LSCF	5.4422(1)	–	13.2549(3)	339.98(1)	–
$Ce_{0.9}Gd_{0.1}O_{1.95}$	CGO	5.4192(1)	–	–	159.15(1)	–

[a] Presence of unreacted La_2O_3.

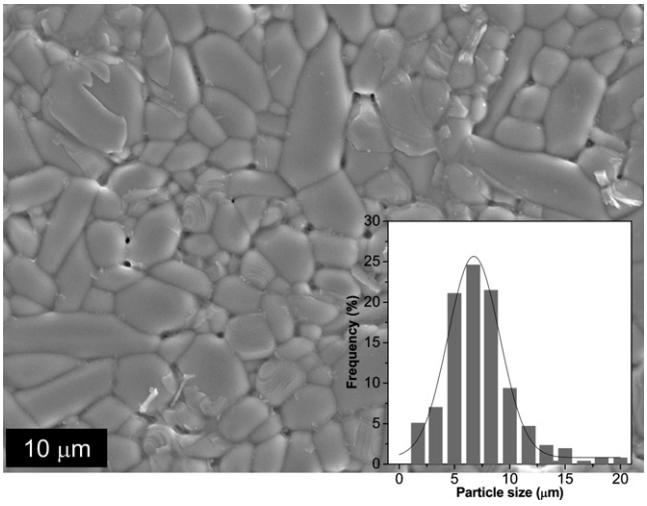

Fig. 1. Scanning electron micrograph of the polished and thermally etched surface of $La_9Sr_1Si_6O_{26.5}$ pellet obtained by reactive sintering at 1650 °C for 10 h. The inset shows the grain size distribution.

the fitting parameters were high, and hence, these values are not reported here. The Arrhenius plot of the overall conductivity is shown in the inset of Fig. 2.

$La_9Sr_1Si_6O_{26.5}$ prepared by reactive sintering at 1650 °C for 10 h gave an overall conductivity of 2.5×10^{-2} S cm^{-1} at 700 °C and 4.3×10^{-2} S cm^{-1} at 800 °C. These conductivity values are somewhat higher than those previously reported for the same electrolyte composition with similar relative density. For instance, Brisse et al. [42] and Bonhomme et al. [24] reported 1.0×10^{-2} S cm^{-1} at 700 °C, for samples prepared by the ceramic method (98–99% TD) at 1575 °C for 2 h and 1500 °C for 8 h, respectively. Orera et al. [43] reported 1.0×10^{-2} S cm^{-1} at 800 °C for a sample prepared by ceramic method (92% TD) at 1600 °C for 2 h. Very recently, Zhang et al. reported a value of 2.4×10^{-2} S cm^{-1} at 800 °C for a sample (97% TD) prepared by a sol–gel method and sintered at 1600 °C for 4 h [44].

Two regimes with different activation energies are observed in the Arrhenius plot, as found for related oxygen-excess oxy-apatite materials [45–47]. This curvature is usually explained by the presence of a critical temperature, T_c [48], below which the charge carriers are progressively trapped, which increases the overall activation energies. The activation energy values are 0.41(1) eV and 0.94(1) eV, in the high and low temperature regimes, respectively.

3.2. Chemical compatibility

The chemical compatibility of $La_9Sr_1Si_6O_{26.5}$ was evaluated by XRPD with the electrode materials listed in Table 1. Powder mixtures of electrolyte and electrodes 1:1 wt.% were calcined at different temperatures and then analyzed at room temperature (Figs. 3–6). The XRPD patterns corresponding to LSM–silicate mixture do not show additional diffraction peaks, associated to reaction products, up to 1000 °C (Fig. 3). Conversely, tiny diffraction peaks are observed at 1100 °C and higher temperatures, which could be assigned to different polymorphs of SiO_2 (quartz and cristobalite). The unit cell volume for the silicate oxy-apatite was determined by Rietveld refinement and it varies from 588.72(4) Å^3 from the initial sample to 588.21(7) Å^3 after firing the mixture at 1300 °C for 24 h, see Table 2. In the same temperature range, the unit cell

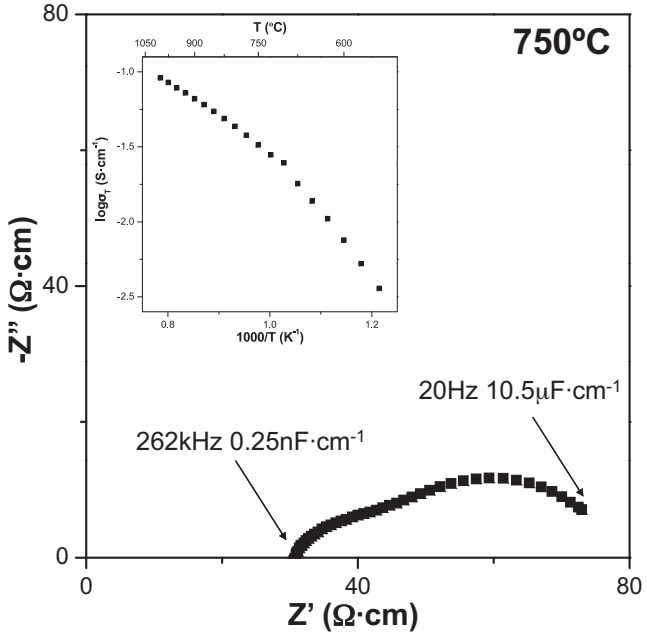

Fig. 2. Complex impedance plane plot for $La_9Sr_1Si_6O_{26.5}$ measured at 750 °C. Selected frequency and capacitance points are highlighted. The inset shows the Arrhenius plot of the overall conductivity.

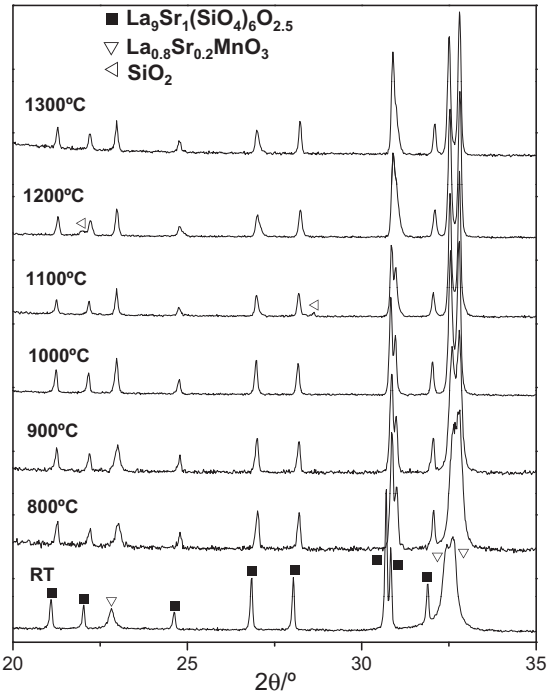

Fig. 3. XRPD patterns for $La_{0.8}Sr_{0.2}MnO_{3-\delta}/La_9Sr_1Si_6O_{26.5}$ powder mixtures (1:1 wt.%) at room temperature (RT) and after firing between 800 and 1300 °C. The different reaction products when increasing temperature are highlighted.

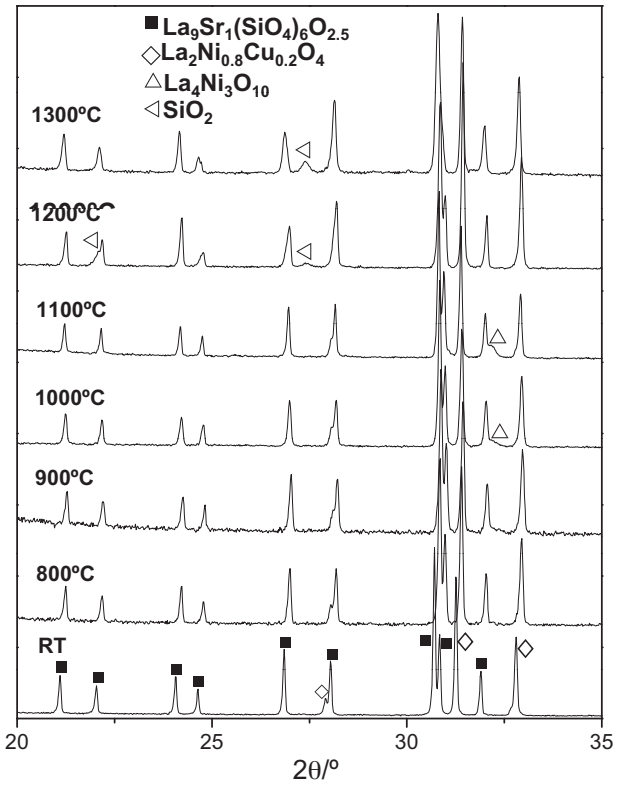

Fig. 4. XRPD patterns for $La_2Ni_{0.8}Cu_{0.2}O_{3-\delta}$/$La_9Sr_1Si_6O_{26.5}$ powder mixtures (1:1 wt.%) at room temperature (RT) and after firing between 800 and 1300 °C. The different reaction products when increasing temperature are highlighted.

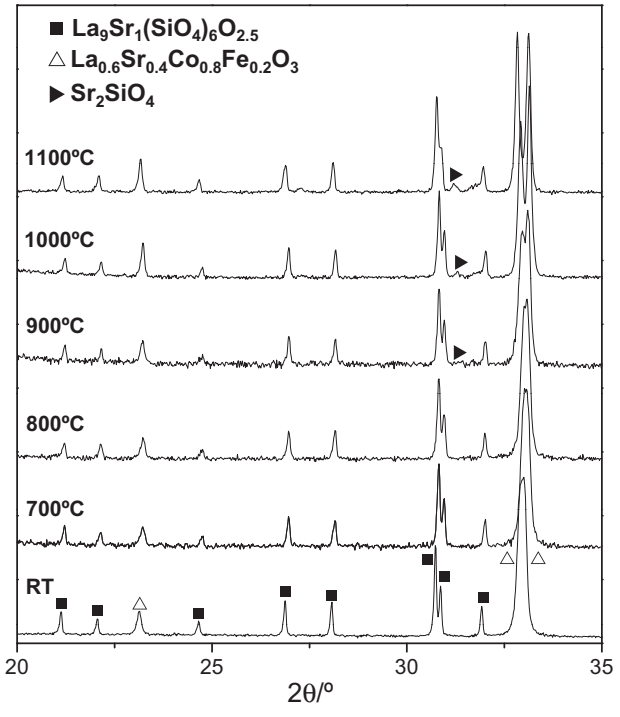

Fig. 5. XRPD patterns for $La_{0.6}Sr_{0.4}Co_{0.8}Fe_{0.2}O_{3-\delta}$/$La_9Sr_1Si_6O_{26.5}$ powder mixtures (1:1 wt.%) at room temperature (RT) and after firing between 700 and 1100 °C. The different reaction products when increasing temperature are highlighted.

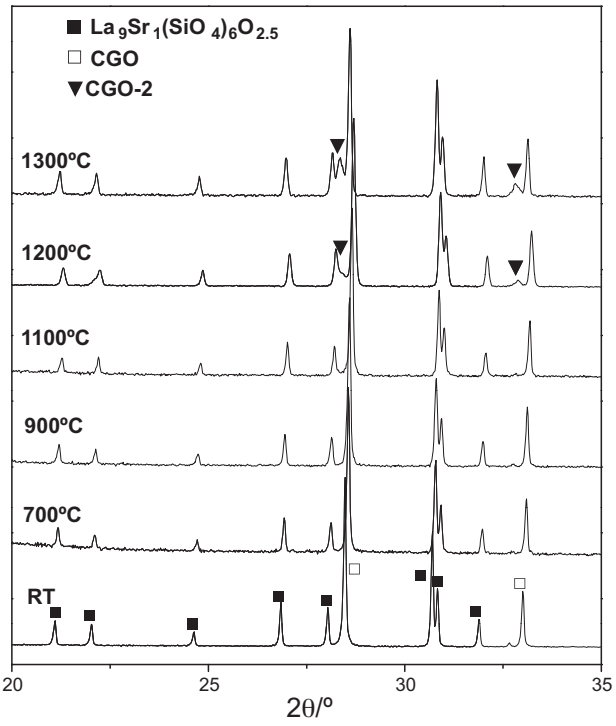

Fig. 6. XRPD patterns for CGO/$La_9Sr_1Si_6O_{26.5}$ powder mixtures (1:1 wt.%) at room temperature (RT) and after firing between 700 and 1300 °C. The different reaction products when increasing temperature are highlighted.

volume for LSM varies from 234.59(2) to 235.66(4) Å^3. The small variation of cell volume for both phases seems to indicate that cation interdiffusion between both materials is not very significant, however the segregation of minor phases at the electrode/electrolyte interface, such as insulating SiO_2, might negatively affect to the electrochemical performance of the this electrode. It should be commented that SiO_2 was not detected by XRPD between $La_{10}Al_{1-x}Si_{6-x}O_{26.5}$ ($x = 0.5$ and 1) and LSM up to 1300 °C in previous works [21,26]. At temperatures higher than 1000 °C a very tiny amount of crystalline SiO_2 is detected which is not observed above 1300 °C. This thermal behaviour may be due to reaction of SiO_2 and/or to volatilization. It should be noted that diffusion of silica in the electrode interface was indeed found by EDS which points to the reaction of silica.

The LNC–silicate mixture after firing at 1000 °C shows the presence of reaction products, identified as $La_4Ni_3O_{10}$ (PDF 035-1242) (Fig. 4). The $La_4Ni_3O_{10}$ with Ruddlesden–Popper type structure is usually used as cathode material in SOFC, and hence, its segregation does not necessarily imply a detrimental effect. The formation of this phase could be explained by lanthanum migration from LNC to the apatite silicate. This seems to be confirmed by the significant change of the cell volume of the silicate with the temperature between 588.72(4) Å^3 at RT to 592.35(4) Å^3 at 1300 °C (Table 2). The diffraction peaks ascribed to $La_4Ni_3O_{10}$ disappear at temperatures above 1200 °C and a significant fraction of silica is observed at 1300 °C. Tsipis et al. [21] previously reported a good compatibility between $La_{10}AlSi_5O_{26.5}$ and $La_2Ni_{0.8}Cu_{0.2}O_4$ up to 1100 °C, however higher sintering temperatures

Table 2
Unit cell volumes (Å^3) of $La_9Sr_1Si_6O_{26.5}$/electrodes (italics) powder mixtures (1:1 wt.% ratio) obtained by Rietveld quantitative phase analyses after firing between 700 and 1300 °C for 24 h in air.

Mixture	700 °C	800 °C	900 °C	1000 °C	1100 °C	1200 °C	1300 °C
$La_9Sr_1Si_6O_{26.5}$	589.10(6)	589.88(8)	590.03(4)	589.66(5)	589.03(7)	588.07(7)	588.21(7)
$La_{0.8}Sr_{0.2}MnO_3$	*234.65(4)*	*234.94(4)*	*235.13(4)*	*234.97(3)*	*234.98(4)*	*235.58(4)*	*235.66(4)*
$La_9Sr_1Si_6O_{26.5}$	589.42(3)	589.54(3)	590.03(4)	589.98(2)	589.77(2)	590.56(3)	592.35(4)
$La_2Ni_{0.8}Cu_{0.2}O_4$	*190.05(2)*	*190.05(1)*	*190.14(1)*	*190.05(1)*	*190.01(1)*	*189.97(1)*	*189.75(1)*
$La_9Sr_1Si_6O_{26.5}$	589.28(5)	589.20(5)	589.55(7)	589.85(4)	589.57(4)	–	–
$La_{0.6}Sr_{0.4}Co_{0.8}Fe_{0.2}O_3$	*340.21(3)*	*340.19(3)*	*341.14(4)*	*341.19(2)*	*340.70(2)*	–	–
$La_9Sr_1Si_6O_{26.5}$	589.12(3)	589.59(3)	589.63(2)	589.77(1)	589.95(2)	589.52(2)	590.63(2)
$Ce_{0.9}Gd_{0.1}O_{1.95}$	*159.25(1)*	*159.32(1)*	*159.28(1)*	*159.31(1)*	*159.40(1)*	*159.38(1)*	*159.58(1)*
$Ce_{0.9}Gd_{0.1}O_{1.95}$-2						*163.39(4)*	*164.59(4)*

result in surface-spreading of silica in the electrode layers near apatite electrolyte. This effect may produce a decrease of the electrochemical reaction zones and consequently the performance of this electrode would decrease. To avoid this drawback the sintering temperature between both materials should be lower than 1200 °C.

The XRPD patterns of the silicate and LSCF mixture show additional diffraction peaks above 900 °C. The reaction product has been identified as Sr_2SiO_4 (PDF 024-1231) (Fig. 5). The amount of reaction products increases with the firing temperature, between 900 and 1100 °C, although its fraction is relatively small compared to the majority phases. The cell volume for the apatite electrolyte increases slightly with the sintering temperature, evolving from 588.72(4) Å^3 at RT to 589.57(4) Å^3 at 1100 °C (Table 2).

The chemical compatibility results obtained herein are very similar to those found in related works [21,26]. The formation of reaction products at the silicate/electrode interface was mainly associated to silica diffusion. In most cases segregation of silica or insulating silicates were observed by XRPD analysis. Hence, the application of silicate-based ionic conductors as solid electrolyte requires suppressing SiO_2 diffusion. A possible alternative to overcome this drawback would be to deposit a protective layer of ceria [26] on the electrolyte surface to prevent interdiffusion of cations. For this reason, the reactivity between the apatite electrolyte and CGO was also investigated.

The XRPD patterns for apatite–CGO mixture do not show any evidence of bulk reactivity below 1100 °C (Fig. 6). However, the diffraction peaks for CGO become asymmetric as the temperature increase and additional diffraction peaks were observed between 1200 and 1300 °C, which were assigned to a new fluorite type structure. The XRPD patterns were analyzed by Rietveld method, considering three different phases: the apatite and two fluorite-type structures with similar cell parameters (see Table 2). The variation of the cell parameters in the mixture as a function of the firing temperature shows that the volume cell for the silicate increases by increasing the temperature. On the contrary, it remains almost constant for the main fluorite-type phase and increase for the minority fluorite-type phase. A possible explanation for this behaviour could be the interdiffusion of cations between CGO and the silicate. Lanthanum migration from the apatite to the fluorite structure would increase the dopant concentration in CGO with the consequent cell volume expansion. Indeed, lanthanum diffusion towards the CGO layer was observed by EDX in the interface CGO/lanthanum silicate [26]. Considering these results, the CGO protective layer should be deposited at

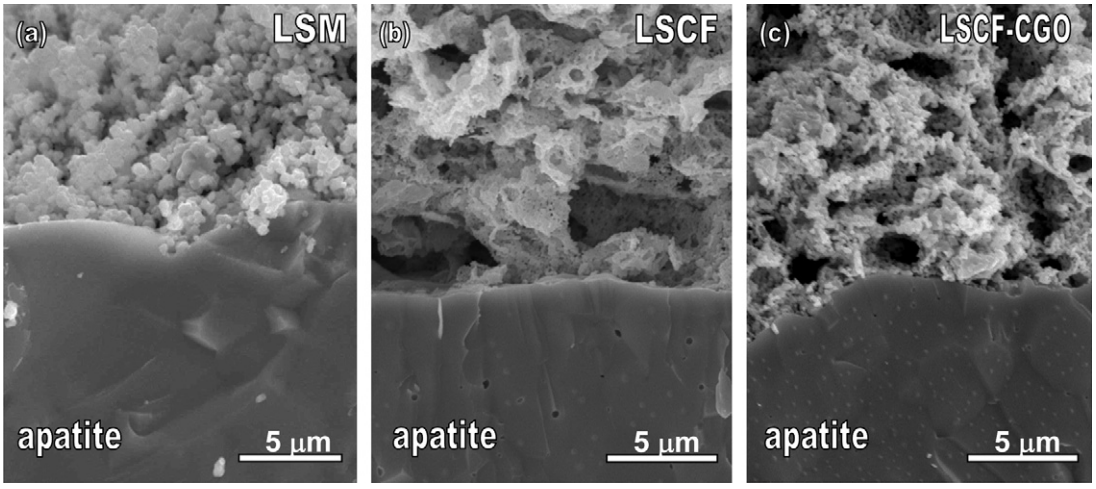

Fig. 7. Cross-section SEM images of electrolyte–electrode interfaces: (a) $La_{0.8}Sr_{0.2}MnO_{3-\delta}/La_9Sr_1Si_6O_{26.5}$, (b) $La_{0.6}Sr_{0.4}Co_{0.8}Fe_{0.2}O_{3-\delta}/La_9Sr_1Si_6O_{26.5}$, and (c) $La_{0.6}Sr_{0.4}Co_{0.8}Fe_{0.2}O_{3-\delta}$–CGO/$La_9Sr_1Si_6O_{26.5}$.

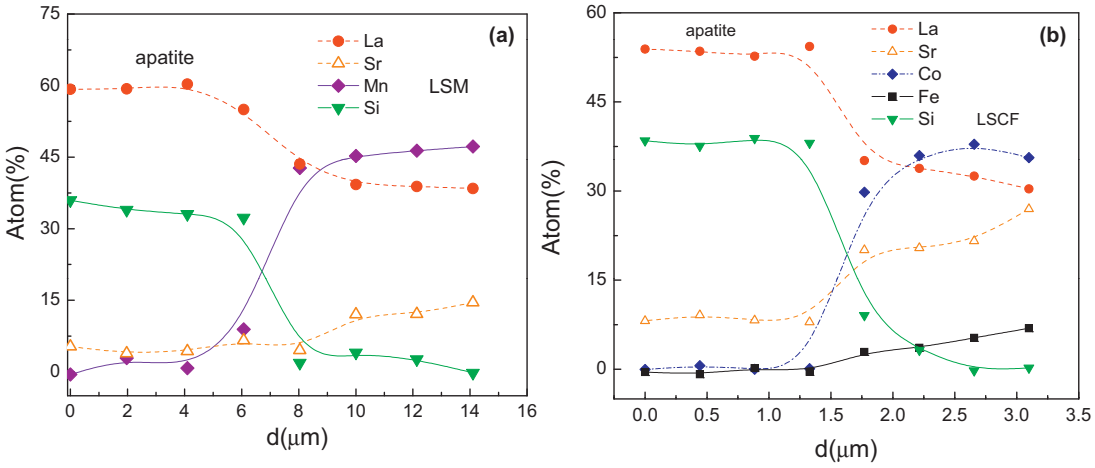

Fig. 8. Variation of the atomic fraction for (a) $La_{0.8}Sr_{0.2}MnO_{3-\delta}/La_9Sr_1Si_6O_{26.5}$ and (b) $La_{0.6}Sr_{0.4}Co_{0.8}Fe_{0.2}O_{3-\delta}/La_9Sr_1Si_6O_{26.5}$ with the distance to the interface.

temperatures as low as possible to avoid cation interdiffusion between the silicate and the CGO layers. Alternative methods such as spray-pyrolysis would allow depositing a thin layer of CGO on the apatite electrolyte at lower temperatures. This will be studied in a forthcoming investigation.

3.3. SEM and EDS analyses

Combined SEM and EDS studies were performed to further investigate the chemical compatibility between the apatite and the electrode materials. The SEM images at the electrode/electrolyte interface, after the electrochemical tests, reveal an adequate adherence between both materials and no evidences of chemical reactivity were detected (Fig. 7a and b). EDS analysis are shown in Fig. 8a and b for LSM and LSCF electrodes, respectively. The variation of the elemental composition across the interfaces does not show a significant interdiffusion of cations between the electrolyte and electrode layers. In addition, the cation composition of the different layers gave similar results to those expected from the nominal stoichiometries within the uncertainty of the technique. This indicates that reactivity occurs very near the electrolyte/electrode interface as previously discussed by Tspisis et al. [21].

3.4. Area specific resistance measurements

The dependence of the area-specific resistance (ASR) with temperature for different electrodes deposited over the $La_9Sr_1Si_6O_{26.5}$ electrolyte is shown in Fig. 9. The processing temperatures vary and were given in Section 2. The LSM cathode exhibits the highest ASR in the whole studied temperature range with a value of 2.3 Ω cm^2 at 800 °C. This value of ASR is comparable to those obtained previously for related silicate oxy-apatites (e.g. 5.5 Ω cm^2 for 40% CGO–LSM [25] and 5.9 Ω cm^2 for LSM using $La_{10}Al_{1-x}Si_{6-x}O_{26.5}$ electrolyte). Note that the values of ASR for the Pt electrodes are higher than those of LSCF which indicates that the electrocatalytic effects of Pt for oxygen reduction are much smaller. The LSCF cathode shows lower ASR values, i.e. 0.56 Ω cm^2 at 800 °C, and it could be ascribed to the highest ionic-electronic conduction in cobaltite compared to manganite-based cathodes and also the lower sintering temperature necessary to obtain an adequate adherence between the electrolyte and electrodes. The values of ASR are notably improved when a composite of LSCF and CGO are used (i.e. 0.1 Ω cm^2 was obtained at 800 °C for 50% CGO–LSCF composite). This effect could be related to the lower reactivity between CGO and apatite silicates at the low sintering temperature used. However, the microstructure is also an important factor to take into account in the electrode performance. The LSCF electrode shows a microstructure formed by particle aggregates with an average grain size lower than 1 μm (Fig. 7b). On the contrary, the LSCF–CGO composite is formed by lower agglomeration of particles and possible better electrochemical performance (Fig. 7c).

In summary, the $La_9Sr_1Si_6O_{26.5}$ electrolyte exhibits relatively high interfacial reactivity with the commonly used

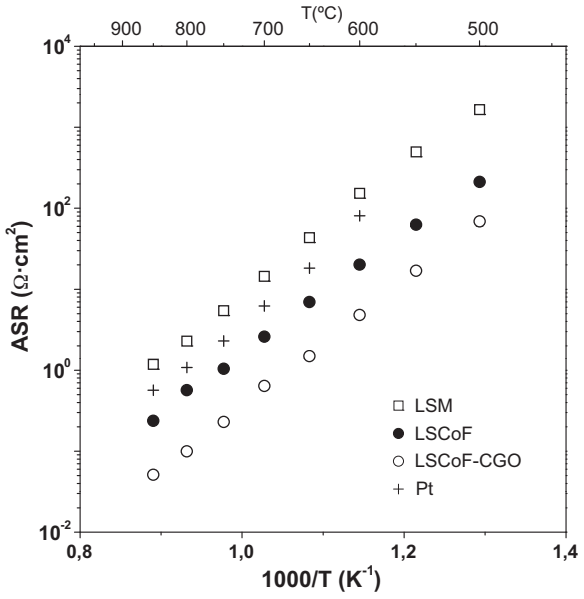

Fig. 9. Temperature dependence of the area-specific resistance (ASR) values for the different cathode materials deposited over the apatite-silicate electrolyte at open circuit voltage.

cathode materials likely due to silica segregation in the electrode/electrolyte interface. The same behaviour was previously observed for related silicate apatites [21,26]. In order to overcome this drawback, the deposition temperature of the electrodes should be as low as possible, or the use of a protective layer (i.e. CGO) between the electrolyte and electrodes must be required. Alternatively, it would be necessary to implement new electrode deposition methods which yield good electrochemical and mechanical properties after processing at lower temperatures.

4. Conclusions

$La_9Sr_1Si_6O_{26.5}$ oxy-apatite has been prepared in a single heating step by reactive sintering. Fully dense pellets, obtained at 1650 °C for 10 h, showed very high oxide-anion conductivity, 25 mS cm^{-1} at 700 °C. The chemical compatibility of this oxy-apatite with three common SOFC cathode materials, $La_{0.8}Sr_{0.2}MnO_3$, $La_2Ni_{0.8}Cu_{0.2}O_4$ and $La_{0.6}Sr_{0.4}Co_{0.8}Fe_{0.2}O_3$, has been investigated. The temperatures that lead to reaction, as observed in the powder diffraction patterns by the appearance of reaction products, were determined to be 1100 °C, 1000 °C and 900 °C, respectively. The segregation of minor amounts of SiO_2 seems to be a key limiting factor that must be overcome by optimising the processing conditions. Furthermore, area specific resistances were determined for these cathode materials deposited over dense oxy-apatite pellets. The LSM exhibits the highest ASR, 2.3 Ω cm^2 at 800 °C. LSCF shows a lower ASR, 0.56 Ω cm^2 at 800 °C. Finally, a 50 wt.% LSCF–CGO composite shows the lowest ASR, 0.1 Ω cm^2 at 800 °C, which is justified by the lower reactivity between CGO and the oxy-apatite as well as the low sintering temperature required to fix this cathode.

Acknowledgements

This work was supported by Junta de Andalucía (Spain) through the P10-FQM-6680 research grant and by Spanish Ministry of Science and Innovation through a Ramón y Cajal fellowship (RYC-2008-03523). JMPV would like to express thanks to Engineering and Physical Sciences Research Council (EPSRC) for funding.

References

[1] R.M. Ormerod, Solid oxide fuel cells, Chem. Soc. Rev. 32 (2003) 17–28.
[2] N.P. Brandon, S. Skinner, B.C.H. Steele, Recent advances in materials for fuel cells, Annu. Rev. Mater. Res. 33 (2003) 183–213.
[3] J.W. Fergus, Electrolytes for solid oxide fuel cells, J. Power Sources 162 (2006) 30–40.
[4] J.W. Fergus, R. Hui, X. Li, D.P. Wilkinson, J. Zhang, Solid Oxide Fuel Cells, Materials Properties and Performance, CRC Press, Taylor & Francis Group, Boca Ratón, FL, 2009.
[5] S. Nakayama, T. Kageyama, H. Aono, Y. Sadaoka, Ionic conductivity of lanthanoid silicates, $Ln_{10}(SiO_4)_6O_3$(Ln = La, Nd, Sm, Gd, Dy, Y, Ho, Er and Yb), J. Mater. Chem. 5 (1995) 1801–1805.
[6] H. Arikawa, H. Nishiguchi, T. Ishihara, Y. Takita, Oxide ion conductivity in Sr-doped $La_{10}Ge_6O_{27}$ apatite oxide, Solid State Ionics 136-137 (2000) 31–37.
[7] E.J. Abram, D.C. Sinclair, A.R. West, A novel enhancement of ionic conductivity in the cation-deficient apatite $La_{9.33}(SiO_4)_6O_2$, J. Mater. Chem. 11 (2001) 1978–1979.
[8] J.E.H. Sansom, D. Richings, P.R. Slater, A powder neutron diffraction study of the oxide-ion-conducting apatite-type phases, $La_{9.33}Si_6O_{26}$ and $La_8Sr_2Si_6O_{26}$, Solid State Ionics 139 (2001) 205–210.
[9] S. Nakayama, M. Sakamoto, M. Higuchi, K. Kodaira, M. Sato, S. Kakita, T. Suzuki, K. Itoh, Oxide ionic conductivity of apatite type $Nd_{9.33}(SiO_4)_6O_2$ single crystal, J. Eur. Ceram. Soc. 19 (1999) 507–510.
[10] P.R. Slater, J.E.H. Sansom, J.R. Tolchard, Development of apatite-type oxide ion conductors, Chem. Rec. 4 (2004) 373–384.
[11] L. León-Reina, E.R. Losilla, M. Martínez-Lara, S. Bruque, M.A.G. Aranda, Interstitial oxygen conduction in lanthanum oxy-apatite electrolytes, J. Mater. Chem. 14 (2004) 1142–1149.
[12] J.R. Tolchard, M.S. Islam, P.R. Slater, Defect chemistry and oxygen ion migration in the apatite-type materials $La_{9.33}Si_6O_{26}$ and $La_8Sr_2Si_6O_{26}$, J. Mater. Chem. 13 (2003) 1956–1961.
[13] M.S. Islam, J.R.Tolchard, P.R. Slater, An apatite for fast oxide ion conduction, Chem. Commun. 148 (2003) 6–1487.
[14] E. Kendrick, M.S. Islam, P.R. Slater, Atomic-scale mechanistic features of oxide ion conduction in apatite-type germanates, Chem. Commun. 71 (2008) 5–717.
[15] L. León-Reina, J.M. Porras-Vázquez, E.R. Losilla, M.A.G. Aranda, Interstitial oxide positions in oxygen-excess oxy-apatites, Solid State Ionics 177 (2006) 1307–1315.
[16] L. León-Reina, J.M. Porras-Vázquez, E.R. Losilla, D.V. Sheptyakov, A. Llobet, M.A.G. Aranda, Low temperature crystal structures of apatite oxygen-conductors containing interstitial oxygen, Dalton Trans. (2007) 2058–2064.
[17] P.J. Panteix, I. Julien, D. Bernache-Assollant, P. Abélard, Synthesis and characterization of oxide ion conductors with the apatite structure for intermediate temperature SOFC, Mater. Chem. Phys. 95 (2006) 313–320.
[18] S. Tao, J.T.S. Irvine, Preparation and characterisation of apatite-type lanthanum silicates by a sol–gel process, Mater. Res. Bull. 36 (2001) 1245–1258.
[19] H. Yoshioka, Oxide ionic conductivity of apatite-type lanthanum silicates, J. Alloys Compd. 408 (2006) 649–652.
[20] (a) A. Chesnaud, G. Dezanneau, C. Estournès, C. Bogicevic, F. Karolak, S. Geiger, G. Geneste, Influence of synthesis route and composition on electrical properties of $La_{9.33+x}Si_6O_{26+3x/2}$ oxy-apatite compounds, Solid State Ionics 179 (2008) 1929–1939;
(b) A. Chesnaud, C. Bogicevic, F. Karolak, C. Estournès, G. Dezanneau, Preparation of transparent oxyapatite ceramics by combined use of freeze-drying and spark-plasma sintering, Chem. Commun. 15 (2007) 1550–1552.
[21] E.V. Tsipis, V.V. Kharton, J.R. Frade, Electrochemical behavior of mixed-conducting oxide cathodes in contact with apatite-type $La_{10}Si_5AlO_{26.5}$ electrolyte, Electrochim. Acta 52 (2007) 4428–4435.
[22] A.A. Yaremchenko, D.O. Bannikov, A.V. Kovalevsky, V.A. Cherepanov, V.V. Kharton, High-temperature transport properties, thermal expansion and cathodic performance of Ni-substituted $LaSr_2Mn_2O_{7-\delta}$, J. Solid State Chem. 181 (2008) 3024–3032.
[23] A.A. Yaremchenko, V.V. Kharton, D.O. Bannikov, D.V. Znosak, J.R. Frade, V.A. Cherepanov, Performance of perovskite-related oxide cathodes in contact with lanthanum silicate electrolyte, Solid State Ionics 180 (2009) 878–885.
[24] C. Bonhomme, S. Beaudet-Savignat, T. Chartier, A. Maître, A-L. Sauvet, B. Soulestin, Sintering kinetics and oxide ion conduction in Sr-doped apatite-type lanthanum silicates, $La_9Sr_1Si_6O_{26.5}$, Solid State Ionics 180 (2009) 1593–1598.
[25] F. Mauvy, C. Lalanne, J-M. Bassat, J-C. Grenier, A. Brisse, A-L. Sauvet, C. Barthet, J. Fouletier, Electrochemical study of the $Nd_{1.95}NiO_{4+\delta}$ oxide electrolyte interface, Solid State Ionics 180 (2009) 1183–1189.
[26] D. Marrero-López, M.C. Martín-Sedeño, J. Peña-Martínez, J.C. Ruiz-Morales, P. Núñez, M.A.G. Aranda, J.R. Ramos-Barrado, J. Power Sources 195 (2010) 2496–2506.
[27] J. Peña-Martínez, D. Marrero-López, J.C. Ruiz-Morales, B.E. Buergler, P. Núñez, L.J. Gauckler, J. Power Sources 159 (2006) 914.

[28] D. Marrero-López, J. Peña-Martínez, J.C. Ruiz-Morales, D. Pérez-Coll, M.C. Martín-Sedeño, P. Núñez, Solid State Ionics 178 (2007) 1366.
[29] D. Marrero-López, J. Peña-Martínez, J.C. Ruiz-Morales, D. Pérez-Coll, M.A.G. Aranda, P. Núñez, Mater. Res. Bull. 8-9 (2008) 2441.
[30] A.C. Larson, R.B.V. Dreele, General Structure Analysis System (GSAS) program. Rep. No. LA-UR-86748. Los Alamos National Laboratory, Los Alamos, CA, 1994.
[31] P. Thompson, D.E. Cox, J.B. Hasting, Rietveld refinement of Debye–Scherrer synchrotron X-ray data from alumina, J. Appl. Crystallogr. 20 (1987) 79.
[32] L.W. Finger, D.E. Cox, A.P. Jephcoat, A correction for powder diffraction peak asymmetry due to axial divergence, J. Appl. Crystallogr. 27 (1994) 892.
[33] winDETA, Novocontrol GmbH, Hundsangen, Germany, 1995.
[34] D. Johnson, ZView: a Software Program for IES Analysis, Version 3.1c, Scribner Associates Inc., Southern Pines, NC, 2007.
[35] Y.C. Liou, K.H. Tseng, Stoichiometric $Pb(Mg_{1/3}Nb_{2/3})O_3$ perovskite ceramics produced by reaction-sintering process, Mater. Res. Bull. 38 (2003) 1351–1357.
[36] Y.C. Liou, C.Y. Shih, C.H. Yu, Stoichiometric $Pb(Fe_{1/2}Nb_{1/2})O_3$ perovskite ceramics produced by reaction-sintering process, Mater. Lett. 57 (2003) 1977–1981.
[37] Y.C. Liou, C.T. Wu, K.H. Tseng, T.C. Chung, Synthesis of $BaTi_4O_9$ ceramics by reaction-sintering process, Mater. Res. Bull. 40 (2005) 1483–1489.
[38] Y.C. Liou, J.H. Chen, H.W. Wang, C.Y. Liu, Synthesis of $(Ba_xSr_{1-x})(Zn_{1/3}Nb_{2/3})O_3$ ceramics by reaction-sintering process and microstructure, Mater. Res. Bull. 41 (2006) 455–460.
[39] Y.C. Liou, W.H. Shiue, C.Y. Shih, Microwave ceramics $Ba_5Nb_4O_{15}$ and $Sr_5Nb_4O_{15}$ prepared by a reaction-sintering process, Mater. Sci. Eng. B 131 (2006) 142–146.
[40] J.M. Porras-Vázquez, E.R. Losilla, L. León-Reina, D. Marrero-López, M.A.G. Aranda, Microstructure and oxide ion conductivity in a dense $La_{9.33}(SiO_4)O_2$ oxyapatite, J. Am. Ceram. Soc. 92 (2009) 1062–1068.
[41] I. Santacruz, J.M. Porras-Vazquez, E.R. Losilla, M.I. Nieto, R. Moreno, M.A.G. Aranda, Colloidal processing and characterization of aluminum-doped lanthanum oxy-apatite, $La_{10}AlSi_5O_{26.5}$, J. Am. Ceram. Soc. 94 (2011) 224–230.
[42] A. Brisse, A.-L. Sauvet, C. Barthet, S. Georges, J. Fouletier, Microstructural and electrochemical characterizations of an electrolyte with an apatite structure, $La_9Sr_1Si_6O_{26.5}$, Solid State Ionics 178 (2007) 1337–1343.
[43] A. Orera, E. Kendrick, D.C. Apperley, V.M. Orera, P.R. Slater, Effect of oxygen content on the ^{29}Si NMR, Raman spectra and oxide ion conductivity of the apatite series, $La_{8+x}Sr_{2-x}(SiO_4)_6O_{2+x/2}$, Dalton Trans. (2008) 5296–5301.
[44] L. Zhang, H.Q. He, H. Wua, C.-Z. Li, S.P. Jiang, Synthesis and characterization of doped $La_9ASi_6O_{26.5}$ (A = Ca, Sr, Ba) oxyapatite electrolyte by a water-based gel-casting route, Int. J. Hydrogen Energy 36 (2011) 6862–6874.
[45] L. León-Reina, M.C. Martín-Sedeño, E.R. Losilla, A. Cabeza, M. Martínez-Lara, S. Bruque, F.M.B. Marques, D.V. Sheptyakov, M.A.G. Aranda, Crystalchemistry and oxide ion conductivity in the lanthanum oxygermanate apatite series, Chem. Mater. 15 (2003) 2099–2108.
[46] L. León-Reina, E.R. Losilla, M. Martínez-Lara, M.C. Martín-Sedeño, S. Bruque, P. Núñez, D.V. Sheptyakov, M.A.G. Aranda, High oxide ion conductivity in Al-doped germanium oxyapatite, Chem. Mater. 17 (2005) 596–600.
[47] L. León-Reina, J.M. Porras-Vazquez, E.R. Losilla, M.A.G. Aranda, Phase transition and mixed oxide-proton conductivity in germanium oxy-apatites, J. Solid State Chem. 180 (2007) 1250–1258.
[48] K. Huang, R.S. Tichy, J.B. Goodenough, Superior perovskite oxide-ion conductor; strontium- and magnesium-doped $LaGaO_3$: I. Phase relationships and electrical properties, J. Am. Ceram. Soc. 81 (1998) 2565–2575.